Catching Conical Intersections in the Act: Monitoring Transient Electronic Coherences by Attosecond Stimulated X-Ray Raman Signals

Markus Kowalewski, Kochise Bennett, Konstantin E. Dorfman, and Shaul Mukamel*
Department of Chemistry, University of California, Irvine, California 92697-2025, USA
(Received 17 June 2015; published 5 November 2015)

Conical intersections (CIs) dominate the pathways and outcomes of virtually all photophysical and photochemical molecular processes. Despite extensive experimental and theoretical effort, CIs have not been directly observed yet and the experimental evidence is being inferred from fast reaction rates and some vibrational signatures. We show that short x-ray (rather than optical) pulses can directly detect the passage through a CI with the adequate temporal and spectral sensitivity. The technique is based on a coherent Raman process that employs a composite femtosecond or attosecond x-ray pulse to detect the electronic coherences (rather than populations) that are generated as the system passes through the CI.

DOI: 10.1103/PhysRevLett.115.193003 PACS numbers: 33.20.-t

Introduction.—The photochemistry of molecules is of considerable fundamental interest with direct impact on synthesis [1], chemical sensors [2], and biological processes [3–7]. Conical intersections (CIs) of electronic states provide a fast, sub-100-femtosecond nonradiative pathway that controls product yields and rates in virtually all photochemical and photophysical processes. At a CI, electronic and nuclear degrees of freedom become strongly coupled and the Born-Oppenheimer approximation, which allowed their separation, breaks down. Strong experimental evidence for CIs is based on the observation of fast conversion rates or other indirect signatures (e.g., suppression of vibrational absorption peaks [8]). However, their direct experimental observation has not been reported yet. The main obstacle is the rapidly decreasing electronic energy gap during the dynamics, requiring an unusual combination of temporal and spectral resolutions which is not available via conventional femtosecond optical and infrared experiments [3,9–11].

We propose a novel, background-free technique that can directly and unambiguously monitor the passage through a CI by using recently developed attosecond broadband x-ray sources. Available optical techniques monitor state populations [3,11] or look for signatures in transient vibrational spectra to identify CIs [8,10,12,13]. The technique proposed in this Letter looks directly at electronic Raman resonances created by the electronic coherence generated as the system passes through the CI and is not sensitive to electronic populations. The time-dependent energy splitting between the two adiabatic surfaces as well as the phase of the wave function can be directly read off the Raman shift between gain and loss features in the Stokes and anti-Stokes signals. Simulations demonstrate how this new method allows the precise timing of when and how a nuclear wave packet reaches and passes through the CI.

TRUECARS.—Any direct measurement of CIs simultaneously requires ultrafast time resolution and adequate spectral resolution in order to resolve the time dependent electronic energy gap. As the nuclei approach a CI from the vertical transition Franck-Condon point of an optical excitation [Fig. 1(a)], they acquire large velocities and the passage through the CI or a seam occurs in a few femtoseconds [9,14–16]. With the ongoing development of free-electron lasers (FELs) [17,18] and high-harmonic-generation (HHG) sources [19], (near transform limited) pulses in the extreme UV to soft x-ray region with a few femtoseconds and down to attosecond durations and several-electron-volt bandwidth [20–24] become available. This makes it possible to directly probe CIs.

The TRUECARS (Transient redistribution of ultrafast electronic coherences in attosecond Raman signals) technique proposed here is a novel extension of time-domain coherent anti-Stokes Raman spectroscopy (CARS) [25–28], commonly used to probe vibrational coherence. In CARS, a pair of optical pulses generates a coherence between vibrational states which is subsequently detected via a Raman process induced by a second pair of pulses. The detected spectrum is displayed versus the time delay T between the two pairs of pulses, revealing the time-dependent vibrational coherence and its dephasing. The temporal and spectral resolution may be enhanced by taking the second pulse pair to be a hybrid pulse—a combination of a narrow-band (picosecond) and a broadband (femtosecond) pulse which is known as hybrid CARS [29,30].

The TRUECARS technique, sketched in Fig. 1, extends hybrid CARS in two important respects: (i) A combination of attosecond or femtosecond x-ray pulses is used to probe electronic coherence rather than conventional optical pulses that probe vibrational coherence. (ii) The coherence is not created directly by applied pulses as in CARS but is generated internally by the propagation through the CI following photoexcitation. A pump pulse first brings the molecule into an excited electronic state, preparing a nonstationary nuclear wave packet which then propagates

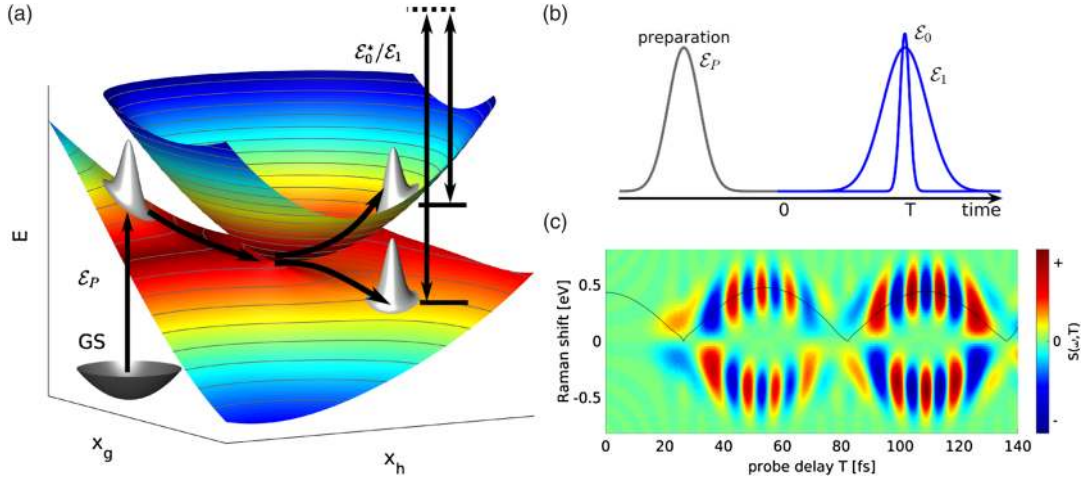

FIG. 1 (color online). Schematic representation of the TRUECARS detection scheme. (a) A nuclear wave packet is promoted from the ground state (GS) by a pump-pulse $\mathcal{E}_P$ to an excited electronic state. As it passes the coupling region around the CI, a coherence is created between the two electronic states. The broadband $\mathcal{E}_0$ or narrow-band $\mathcal{E}_1$ hybrid pulse probes the electronic coherence between the nuclear wave packets on different surfaces. (b) Schematics of the pump and hybrid-probe pulse sequence. (c) Illustration of the signal calculated for a one-dimensional nuclear model. The energy splitting of the electronic states involved in the coherence (solid line) can be read from the Raman shift.

towards the CI. The electronic coherence is not generated directly by the pulse but instead builds up during the time evolution of the wave packet as it approaches the vicinity of the CI where the nonadiabatic intersurface coupling is present. A hybrid broadband or narrow-band x-ray pulse then probes this electronic coherence by the time-resolved gain and loss of the positive and negative stimulated Raman components [see Fig. 1(b) for depictions of the pulse sequence]. Resolving the entire spectrum of electronic Raman transitions [Fig. 1(c)] requires pulses with a few-electronvolt bandwidth and observing the CI dynamics requires pulses with a duration on the order of few femtoseconds or less. Only x-ray pulses provide the necessary temporal and spectral profiles to detect electronic coherences.

The molecule is coupled to the intensity of the off-resonant probing fields via the electronic polarizability operator $\hat{\alpha}$. The matter-probe interaction Hamiltonian is

$$\hat{H}_{\mathrm{mp}}(t) = \hat{\alpha}|\mathcal{E}_0(t) + \mathcal{E}_1(t)|^2 \tag{1}$$

where $\mathcal{E}_0$ and $\mathcal{E}_1$ are the attosecond (broadband) and femtosecond (narrow-band) components, respectively, of the probing field. The off-resonant electronic polarizability $\hat{\alpha}$ is the transition polarizability describing the Raman transitions between valence states (this is technically frequency dependent but taken to be flat over the relevant range of frequencies since we are in the off-resonant regime). We assume that the dominant transition dipole moments contributing to $\hat{\alpha}$ are core-to-valence transitions. We do not include the photoionization processes in the simulations. It has been experimentally shown that x-ray Raman signals can successfully compete with the ionization background [31,32]. To simplify the analysis, we assume both components to have the same carrier frequency ω_1. The TRUECARS signal is defined as the frequency-dispersed photon number change of the attosecond field and is given by

$$S(\omega, T) = 2\Im \int_{-\infty}^{+\infty} dt e^{i\omega(t-T)} \mathcal{E}_0^*(\omega)\mathcal{E}_1(t-T) \times \langle \psi(t)|\hat{\alpha}|\psi(t)\rangle \tag{2}$$

where T is the time delay between the probe field and the preparation pulse and $|\psi(t)\rangle$ is the total (nuclear and electronic) wave function. The probing fields are assumed to be temporally well separated from the preparation process. The signal carries a phase factor $e^{i(\phi_1-\phi_0)}$, where ϕ_i is the phase of the field $\mathcal{E}_i$. This factor causes the signal to vanish when averaged over random pulse phases; observation of TRUECARS therefore requires control of the relative pulse phases. Note that terms corresponding to electronic populations do not contribute since they carry no dynamical phase and vanish when taking the imaginary part in Eq. (2). TRUECARS therefore provides a background-free measurement of electronic coherence. It is also important to note that, due to the frequency dispersion of the broadband pulse $\mathcal{E}_0(\omega)$, the field-matter interaction time is limited by the femtosecond pulse envelope $\mathcal{E}_1$. The temporal and spectral resolutions of the technique are not independent but are Fourier-conjugate pairs, both determined by the corresponding temporal and spectral profiles of the femtosecond pulse $\mathcal{E}_1$. In order to resolve the changing energy gap along the CI, $\mathcal{E}_1$ must be shorter than the dynamics while spectrally narrower than any relevant

energy splitting. For example, resolving a 0.1 eV energy difference implies at least a 6.5 fs pulse duration so dynamics faster than this will not be resolved.

The pulse configuration in TRUECARS is identical to transient absorption. The difference is that the probe pulse is not resonant with any material transitions and is therefore not absorbed. Instead, there is an oscillatory redistribution of intensity between loss [positive Stokes (negative anti-Stokes)] and gain [positive anti-Stokes (negative Stokes)] that can affect the frequency-resolved transient intensity. The signal is linear in the probe intensity $\mathcal{E}_0\mathcal{E}_1$. Stimulated Raman spectroscopy (SRS) [33–37] uses the same pulse sequence but detects the quadratic signal $\mathcal{E}_0^2\mathcal{E}_1^2$. TRUECARS is therefore phase dependent whereas SRS is phase independent. The quadratic signal would allow greater resolution, since temporal and spectral resolution could then be set by the broadband and narrowband pulses, respectively, and would not be Fourier limited [34]. However, the quadratic signal is typically dominated by contributions stemming from electronic populations [38] and it is not therefore a background-free measurement of the electronic coherence. The linear TRUECARS signal is therefore a much cleaner way to measure the passage through a conical intersection.

Qualitative understanding of the TRUECARS signal can be facilitated by a semiclassical picture. We expand the electronic wave function in the adiabatic basis and assume that the nuclei follow the classical equations of motion:

$$|\psi(t)\rangle = \sum_a c_a(t) e^{-i\int_{-\infty}^{t}\varepsilon_a(\tau)d\tau}|a(t)\rangle, \tag{3}$$

where the instantaneous states $|a(t)\rangle$ and energies $\varepsilon_a(t)$ vary with time through their dependence on the nuclei while the coefficients $c_a(t)$ vary due to the nonadiabatic coupling between the electronic surfaces near CIs. The coherence between the surfaces thus propagates with a time-dependent dynamical phase which generates oscillations in T with evolving period and frequency (ω_r). The energy splitting between the electronic states can thus be read not only from ω_r but also from the oscillation period in T [as can be seen by inserting Eq. (3) into (2)].

To clearly point out the unique features of the TRUECARS signal, Fig. 1(c) shows a simulation of a single vibrational mode with a long electronic coherence time. The model is constructed from two electronic states, which are represented by two displaced harmonic potentials and a Gaussian diabatic coupling. This model can represent, e.g., a simple diatomic molecule with an avoided crossing. A full quantum dynamical wave packet calculation is carried out on a numerical grid with a displaced Gaussian wave packet as the initial condition and the TRUECARS spectrum is calculated according to Eq. (2). In the absence of electronic coherence, the signal vanishes [this is the case in the beginning of the dynamics, Fig. 1(c)]. As the wave packet approaches the nonadiabatic coupling region, an electronic coherence builds up and the signal appears. After it has passed the intersection, the splitting between the states increases again. The signal shows an oscillation of gain and loss features in the Stokes and anti-Stokes regime. The energy splitting (solid line) can be read directly from the Raman shift $\omega_r = \omega - \omega_1$. The broadening of the signal in ω_r is caused by the nonvanishing width of the nuclear wave packet, which covers a range of the finite width of the potential energy surface. The signal builds up on both red ($\omega_r < 0$) and blue ($\omega_r > 0$) sides of the spectrum, appearing as two oscillating peaks. When the red side is positive and the blue side negative, the energy flows from the pulse to the molecule and the process is of Stokes type while opposite conditions yield an anti-Stokes process. The interaction with the molecule thus redistributes the field photons, either shifting the probe pulse toward the red or the blue side of the spectrum, but the total number of photons is conserved [39]. This is due to the off-resonant nature of the Raman probe used here (there is no absorption or stimulated emission) and is the origin of the "redistribution" in TRUECARS. This also leads to the absence of a Rayleigh peak at $\omega_r = 0$, which would come from electronic populations, making the signal background-free (induced only by electronic coherences). The signal oscillates with time T back and forth between Stokes and anti-Stokes and the oscillation period corresponds to the coherence period (the oscillations speed up and the positions of the peaks in the frequency spread apart mirroring the separation of potential energy surfaces). The oscillation period in T therefore also reveals the separation of adiabatic potential energy surfaces, while the magnitude of the signal envelope reveals the decay of the electronic coherence.

Simulations and discussion.—We now demonstrate the power of TRUECARS by wave packet simulation on a more realistic model system with two vibrational modes and two electronic states S_1 and S_2 and typical molecular parameters [depicted schematically in Fig. 1(a)]. This is the minimal model required to describe a CI [40]. The two coordinates resemble the branching space of a CI and are displacements along the derivative coupling vector x_h and the gradient difference vector x_g. The initial condition is at the Franck-Condon point, chosen to be in the vicinity of the CI to allow the wave packet to reach the CI in a short period of time. Examples of molecules with ultrafast nonadiabatic dynamics include cyclohexadiene [41], ethylene [14], pyrazine [9], and DMABN [16]. The wave packet simulations are carried out numerically on a grid in the electronic and nuclear space using the diabatic basis and are transformed into the adiabatic basis as needed. The details of the calculations are given in the Supplemental Material [42].

The molecule is assumed to be initially in its electronic ground state (S_0). An actintic pump pulse creates an

excitation in the S_2 state, thus launching the dynamics. The diabatic coupling vanishes in the Franck-Condon region to allow for an initial condition in which the Born-Oppenheimer approximation holds. The initial S_1/S_2 splitting at the Franck-Condon point is around 2 eV. The wave packet propagates freely on the S_2 surface in the branching space and approaches the CI. The resulting TRUECARS signal [Eq. (2)] and the averaged time-dependent energy splitting is shown in Fig. 2(a) (solid line). The qualitative features are similar to the signal from the diatomic model shown in Fig. 1(c). The prepared state contains no electronic coherence and the signal turns on at around 2 fs, when the system approaches the nonadiabatic coupling region. The corresponding molecular property governing the signal, the off-resonant transition polarizability $\alpha(t)$, is shown in Fig. 2(b). If the $\hat{\alpha}$ is assumed to be independent of the nuclear coordinates, $\alpha(t)$ is directly proportional to the real part of the electronic coherence. In Fig. 2(c), the adiabatic populations are shown along with the magnitude of the electronic coherence. After the wave packet has passed the CI at around 6 fs, it travels through a coordinate region where there is a small but finite splitting between adiabatic potential energy surfaces. The signal broadening stems from two contributions: The width of the nuclear wave packet, covering a certain range of potential energy differences, and the spectral width of the probe pulse. The peak maxima are slightly shifted to larger Raman shifts due to the fact the signal vanishes at $\omega_r = 0$ [an effect that is more pronounced for smaller ω_r as is seen for $T < 12$ fs in Fig. 2(a)]. Additionally the information about the energy splitting is also contained in the oscillations in T, indicating that the system is in close vicinity of the CI, as the oscillation frequency is lowered. At around 15 fs, the energy splitting increases again as can be seen from ω_r. Since the S_1 and S_2 states have different gradients, the overlap between the nuclear wave packets $\langle\Psi_1|\Psi_2\rangle$ decays and the signal fades out. As can be seen in Fig. 2, the passage through the CI happens in less than 12 fs. By utilizing 1.2 fs pulses, the wave packet's arrival at the CI can be timed stroboscopically to within 10 fs. Note that an even shorter coherence lifetime would not allow for a clear determination of the energy splitting, but would increase the time resolution. As is clear from the overlay of the energy splitting on the TRUECARS spectra, the technique is capable of mapping out the potential energy surfaces of the reaction coordinate near the CI. It thus gives both dynamical information on the temporal and spectral profile of the CI by providing information about period of oscillations as well as the phase of the electronic coherences near the CI. TRUECARS might also be useful to measure the Berry phase [47], which so far has eluded detection in chemical systems.

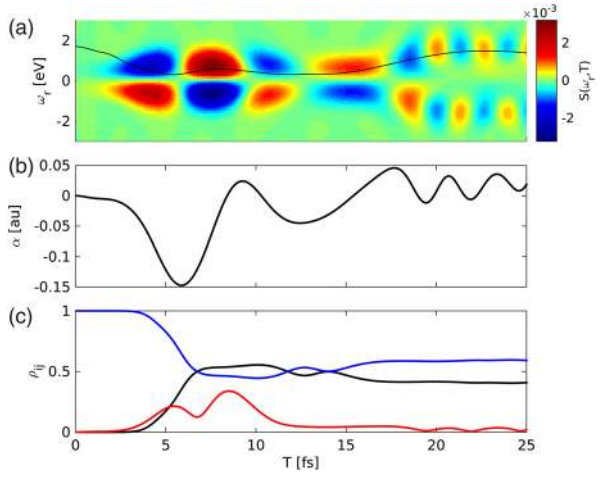

FIG. 2 (color online). (a) Simulated TRUECARS signal [Eq. (2)] for the two-dimensional nuclear model with a pulse length of 1.2 fs ($\mathcal{E}_1$). The solid line indicates the average splitting of the potential energy surfaces. (b) The time dependent expectation value of the polarizability. (c) Elements of the reduced density matrix of the electronic subsystem. Blue and black lines: populations of the adiabatic S_2 and S_1 state respectively. Red line: the magnitude of the electronic coherence.

In summary, we have presented a new spectroscopic technique (TRUECARS) that can directly monitor passage through conical intersections. The technique measures the frequency-resolved stimulated Raman scattering of a probe pulse as a function of the time delay T with respect to the pump pulse. In contrast to existing methods, TRUECARS is only sensitive to electronic coherences and populations do not contribute, making it uniquely suited to probing passage through CIs by capturing the electronic coherences generated by nonadiabatic couplings in the CI vicinity. We simulated the signal for 1D and 2D vibrational model systems and demonstrated that TRUECARS with attosecond pulses can be used to measure the time-varying energy gap between two electronic states. The rapidly decreasing energy gap around the CI is fully visible in the time resolved spectrum. The decay of the electronic coherences contains information about the difference of the gradients between the electronic states, giving a hint about the geometry of the CI. To precisely time the CI and map the energy differences, a molecular system has to pass a CI which is in close vicinity to the Franck-Condon point. This makes TRUECARS an ideal tool to investigate ultrafast, photophysical system dynamics. The experimental parameters required—broadband sub-femtosecond pulses of ~100 eV or more and spectral widths of several eV—could be realized in the near future from state of the art free-electron laser sources [18,48].

The support of the Chemical Sciences, Geosciences, and Biosciences division, Office of Basic Energy Sciences, Office of Science, U.S. Department of Energy through Award No. DE-FG02-04ER15571 as well as from the National Science Foundation (Grant No CHE-1361516) is gratefully acknowledged. The computational resources and the support for Kochise Bennett was provided by

DOE. M. K. gratefully acknowledges support from the Alexander von Humboldt foundation through the Feodor Lynen program.

M. K. and K. B. contributed equally to this work.

*smukamel@uci.edu

[1] P. von den Hoff, S. Thallmair, M. Kowalewski, R. Siemering, and R. de Vivie-Riedle, Phys. Chem. Chem. Phys. **14**, 14460 (2012).
[2] M. F. Garcia-Parajo, Nat. Photonics **2**, 201 (2008).
[3] D. Polli, P. Altoe, O. Weingart, K. M. Spillane, C. Manzoni, D. Brida, G. Tomasello, G. Orlandi, P. Kukura, R. A. Mathies, M. Garavelli, and G. Cerullo, Nature (London) **467**, 440 (2010).
[4] S. Rinaldi, F. Melaccio, S. Gozem, F. Fanelli, and M. Olivucci, Proc. Natl. Acad. Sci. U.S.A. **111**, 1714 (2014).
[5] M. Barbatti, G. Granucci, M. Persico, M. Ruckenbauer, M. Vazdar, M. Eckert-Maksić, and H. Lischka, J. Photochem. Photobiol. A **190**, 228 (2007).
[6] M. Barbatti, A. J. A. Aquino, J. J. Szymczak, D. Nachtigallová, P. Hobza, and H. Lischka, Proc. Natl. Acad. Sci. U.S.A. **107**, 21453 (2010).
[7] A. L. Sobolewski, W. Domcke, C. Dedonder-Lardeux, and C. Jouvet, Phys. Chem. Chem. Phys. **4**, 1093 (2002).
[8] A. Raab, G. A. Worth, H. D. Meyer, and L. S. Cederbaum, J. Chem. Phys. **110**, 936 (1999).
[9] T. Horio, T. Fuji, Y.-I. Suzuki, and T. Suzuki, J. Am. Chem. Soc. **131**, 10392 (2009).
[10] T. A. A. Oliver, N. H. C. Lewis, and G. R. Fleming, Proc. Natl. Acad. Sci. U.S.A. **111**, 10061 (2014).
[11] B. K. McFarland, J. P. Farrell, S. Miyabe, F. Tarantelli, A. Aguilar, N. Berrah, C. Bostedt, J. D. Bozek, P. H. Bucksbaum, J. C. Castagna, R. N. Coffee, J. P. Cryan, L. Fang, R. Feifel, K. J. Gaffney, J. M. Glownia, T. J. Martinez, M. Mucke, B. Murphy, A. Natan, T. Osipov, V. S. Petrović, S. Schorb, T. Schultz, L. S. Spector, M. Swiggers, I. Tenney, S. Wang, J. L. White, W. White, and M. Gühr, Nat. Commun. **5**, 4235 (2014).
[12] H. Timmers, Z. Li, N. Shivaram, R. Santra, O. Vendrell, and A. Sandhu, Phys. Rev. Lett. **113**, 113003 (2014).
[13] M. Kowalewski and S. Mukamel, J. Chem. Phys. **143**, 044117 (2015).
[14] H. Tao, T. K. Allison, T. W. Wright, A. M. Stooke, C. Khurmi, J. van Tilborg, Y. Liu, R. W. Falcone, A. Belkacem, and T. J. Martinez, J. Chem. Phys. **134**, 244306 (2011).
[15] S. Patchkovskii and M. S. Schuurman, J. Phys. Chem. A **118**, 12069 (2014).
[16] M. A. Kochman, A. Tajti, C. A. Morrison, and R. J. D. Miller, J. Chem. Theory Comput. **11**, 1118 (2015).
[17] Y. Ding, Z. Huang, D. Ratner, P. Bucksbaum, and H. Merdji, Phys. Rev. ST Accel. Beams **12**, 060703 (2009).
[18] W. Helml, A. R. Maier, W. Schweinberger, I. Grguraš, P. Radcliffe, G. Doumy, C. Roedig, J. Gagnon, M. Messerschmidt, S. Schorb, C. Bostedt, F. Grüner, L. F. DiMauro, D. Cubaynes, J. D. Bozek, T. Th., J. T. Costello, M. Meyer, R. Coffee, S. Düsterer, A. L. Cavalieri, and R. Kienberger, Nat. Photonics **8**, 950 (2014).
[19] T. Popmintchev, M.-C. Chen, P. Arpin, M. M. Murnane, and H. C. Kapteyn, Nat. Photonics **4**, 822 (2010).
[20] M. Harmand *et al.*, Nat. Photonics **7**, 215 (2013).
[21] I. Grguraš *et al.*, Nat. Photonics **6**, 852 (2012).
[22] C. Bostedt *et al.*, J. Phys. B **46**, 164003 (2013).
[23] T. Popmintchev *et al.*, Science **336**, 1287 (2012).
[24] C. Manzoni, O. D. Mücke, G. Cirmi, S. Fang, J. Moses, S.-W. Huang, K.-H. Hong, G. Cerullo, and F. X. Kärtner, Laser Photonics Rev. **9**, 129 (2015).
[25] A. Laubereau and W. Kaiser, Rev. Mod. Phys. **50**, 607 (1978).
[26] K. Yoshihara, R. Inaba, H. Okamoto, M. Tasumi, K. Tominaga, and N. K. A., in *Femtosecond Reaction Dynamics*, edited by W. D. A. (North-Holland, Amsterdam, 1994), pp. 299–310.
[27] T. Ideguchi, S. Holzner, B. Bernhardt, G. Guelachvili, N. Picqué, and T. W. Hänsch, Nature (London) **502**, 355 (2013).
[28] H. Frostig, T. Bayer, N. Dudovich, Y. C. Eldar, and Y. Silberberg, Nat. Photonics **9**, 339 (2015).
[29] D. Pestov, X. Wang, G. O. Ariunbold, R. K. Murawski, V. A. Sautenkov, A. Dogariu, A. V. Sokolov, and M. O. Scully, Proc. Natl. Acad. Sci. U.S.A. **105**, 422 (2008).
[30] J. D. Miller, S. Roy, M. N. Slipchenko, J. R. Gord, and T. R. Meyer, Opt. Express **19**, 15627 (2011).
[31] S. Miyabe and P. Bucksbaum, Phys. Rev. Lett. **114**, 143005 (2015).
[32] C. Weninger, M. Purvis, D. Ryan, R. A. London, J. D. Bozek, C. Bostedt, A. Graf, G. Brown, J. J. Rocca, and N. Rohringer, Phys. Rev. Lett. **111**, 233902 (2013).
[33] M. Yoshizawa and M. Kurosawa, Phys. Rev. A **61**, 013808 (1999).
[34] P. Kukura, D. W. McCamant, and R. A. Mathies, Annu. Rev. Phys. Chem. **58**, 461 (2007).
[35] Z. Sun, J. Lu, D. H. Zhang, and S.-Y. Lee, J. Chem. Phys. **128**, 144114 (2008).
[36] B. P. Fingerhut, K. E. Dorfman, and S. Mukamel, J. Chem. Theory Comput. **10**, 1172 (2014).
[37] F. Bencivenga, R. Cucini, F. Capotondi, A. Battistoni, R. Mincigrucci, E. Giangrisostomi, A. Gessini, M. Manfredda, I. P. Nikolov, E. Pedersoli, E. Principi, C. Svetina, P. Parisse, F. Casolari, M. B. Danailov, M. Kiskinova, and C. Masciovecchio, Nature (London) **520**, 205 (2015).
[38] W. Hua, S. Oesterling, J. D. Biggs, Y. Zhang, H. Ando, R. de Vivie-Riedle, B. P. Fingerhut, and S. Mukamel, Struct. Dyn. **3**, 023601 (2016).
[39] K. E. Dorfman, K. Bennett, and S. Mukamel, Phys. Rev. A **92**, 023826 (2015).
[40] W. Domcke, D. Yarkony, and H. Köppel, *Conical Intersections: Electronic Structure, Dynamics and Spectroscopy*, Vol. 15 (World Scientific, Singapore, 2004).
[41] H. Tamura, S. Nanbu, T. Ishida, and H. Nakamura, J. Chem. Phys. **124**, 084313 (2006).
[42] See Supplemental Material at http://link.aps.org/supplemental/10.1103/PhysRevLett.115.193003 for a detailed description of the quantum dynamics simulations, which includes Refs. [43–46].
[43] A. M. D. Lee, J. D. Coe, S. Ullrich, M. L. Ho, S. J. Lee, B. M. Cheng, M. Z. Zgierski, I. C. Chen, T. J. Martinez, and A. Stolow, J. Phys. Chem. A **111**, 11948 (2007).

[44] H.-J. Werner *et al.*, Molpro, version 2010.1, a package of *ab initio* programs (2010), see http://www.molpro.net.

[45] D. J. Tannor, *Introduction to Quantum Mechanics: A Time-Dependent Perspective* (University Science Books, Sausalito, Calif, 2006).

[46] S. Rahav and S. Mukamel, Adv. At. Mol. Opt. Phys. **59**, 223 (2010).

[47] D. Xiao, M.-C. Chang, and Q. Niu, Rev. Mod. Phys. **82**, 1959 (2010).

[48] S. Huang, Y. Ding, Z. Huang, and J. Qiang, Phys. Rev. ST Accel. Beams **17**, 120703 (2014).

Catching Conical Intersections in the Act; Monitoring Transient Electronic Coherences by Attosecond Stimulated X-Ray Raman Signals

- Supplementary Material -

Markus Kowalewski, Kochise Bennett, Konstantin E. Dorfman, and Shaul Mukamel

I. MODEL SYSTEM

A. 1D-Model System for Signal Shown in Fig. 1(d)

To show the basic feature of the signal a harmonic one dimensional setup has been used. The diabatic potential energy curves are given by two displaced parabolas. All quantities are given in atomic units ($\hbar = m_e = 4\pi\epsilon_0 = 1$).

$$H_1 = \frac{1}{2} 0.01 \left(x - 0.2\right)^2 \tag{S1}$$

$$H_2 = \frac{1}{2} 0.01 \left(x + 0.2\right)^2 \tag{S2}$$

The diabatic coupling is given by a Gaussian function

$$H_{12} = 0.01 \exp\left(-x^2\right) , \tag{S3}$$

representing an avoided crossing. The reduced mass of the system is assumed to be $m = 5100$. The wave packet simulations and the signal calculation is analogous to the two-dimensional model described in Sec. II and III.

B. 2D Model System (Fig. 2)

We use a two-dimensional model system inspired by the S_2-S_1 CoIn in acrolein [1]. The system has been chosen as a role model to obtain realistic parameters for the energy splittings between the PESs and the couplings. The adiabatic and diabatic states were calculated in the vinicinty of the CoIn with the program package MOLPRO [2] at the CASSCF(6/5)/6-31+G* level of theory. The two coordinates of the system, x_h and x_g, correspond to the orthonormal versions of the derivative coupling vector and the gradient difference vector respectively. The diabatic potential energy surfaces and the diabatic couplings have been calculated on a 9×9 grid with maximum displacements of ±0.4. The CoIn is in the origin of the coordinate system. The resulting data is fitted to a third order polynomial:

$$f(x_h, x_g) = c_{00} + c_{10}x_h + c_{01}x_g + c_{20}x_h^2 + c_{11}x_h x_g + c_{02}x_g^2 + c_{30}x_h^3 + c_{21}x_h^2 x_g + c_{12}x_h x_g^2 + c_{03}x_g^3 \tag{S4}$$

The respective parameter sets c_{ij} for H_1, H_2 and H_{12} are given in tab. I. The polynomial allows for extrapolation of the data to a wider parameter range, necessary to run the wave

TABLE I. Parameters for the Polynomial expansions of the diabatic states of the two dimensional model. and couplings (given in atomic units).

Surf.	c_{00}	c_{10}	c_{01}	c_{20}	c_{11}	c_{02}	c_{30}	c_{21}	c_{12}	c_{03}
H_1	-0.001854	-0.02817	-0.114	0.3156	-0.1576	0.2457	0.1237	0.2883	-0.2856	0.1071
H_2	-0.001247	0.01804	0.02297	0.4546	-0.2419	0.2242	0.2404	0.1135	-0.3448	0.07928
H_{12}	0.0006653	-0.05699	-0.001481	-0.02017	-0.06204	0.02157	0.06652	0.05527	0.04719	0.02031

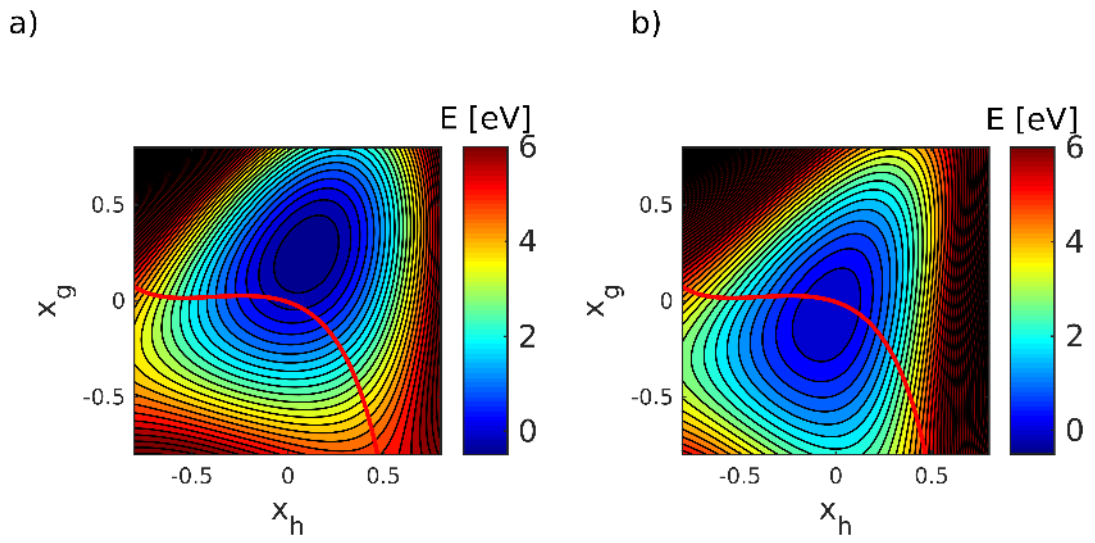

FIG. S1. Diabatic potential energy surfaces a) H_1 and b) H_2. The conical intersection is in the center of the coordinate system. The red line indicates the intersection between both surfaces in the diabatic representation.

packet simulations. The resulting diabatic surfaces, denoted by H_1 and H_2, are shown in Fig. S1. The diabatic coupling H_{12} is created by eq. S4 and shaped by gaussian functions.

$$H_{12} = f(x_h, x_g)h(x_h)\exp\left(\frac{-x_g^2}{0.08}\right) \tag{S5}$$

where $h(x_h)$ is

$$h(x_h) = \begin{cases} \exp\left(-\dfrac{x_h^2}{0.18}\right) & x_h < 0 \\ \exp\left(-\dfrac{x_h^2}{0.045}\right) & x_h \geq 0 \end{cases} \tag{S6}$$

The Gaussian envelope lets the diabatic coupling term vanish in areas far from the CoIn and diabatic states become identical to the adiabatic states. The resulting coupling function is

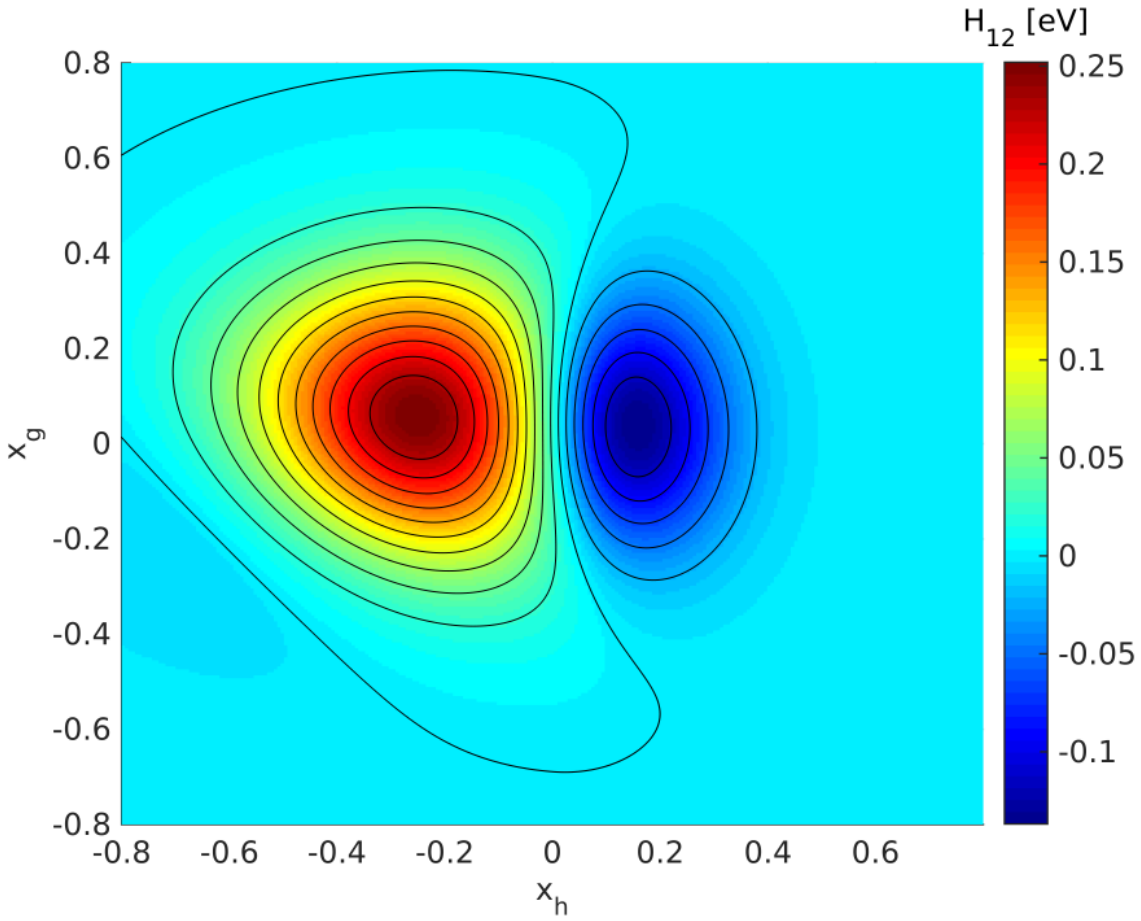

FIG. S2. Contourplot of the diabatic coupling element H_{12}.

shown in Fig. S2. The corresponding adiabatic PESs are readily obtained by diagonalization of the diabatic surfaces (Fig. S3).

II. VIBRONIC WAVE PACKET SIMULATIONS

The wave packet simulations are carried out on the diabatic surfaces by solving the time dependent Schrödinger equation numerically on a position space grid by the Fourier method [3]. The corresponding Hamiltonian in the diabatic representation reads:

$$H = -\mathbb{1}\frac{1}{2m}\sum_{i\in\{h,g\}}\frac{\mathrm{d}^2}{\mathrm{d}x_i^2} + \begin{pmatrix} H_1(x) & H_{12}(x) \\ H_{12}(x) & H_2(x) \end{pmatrix} \tag{S7}$$

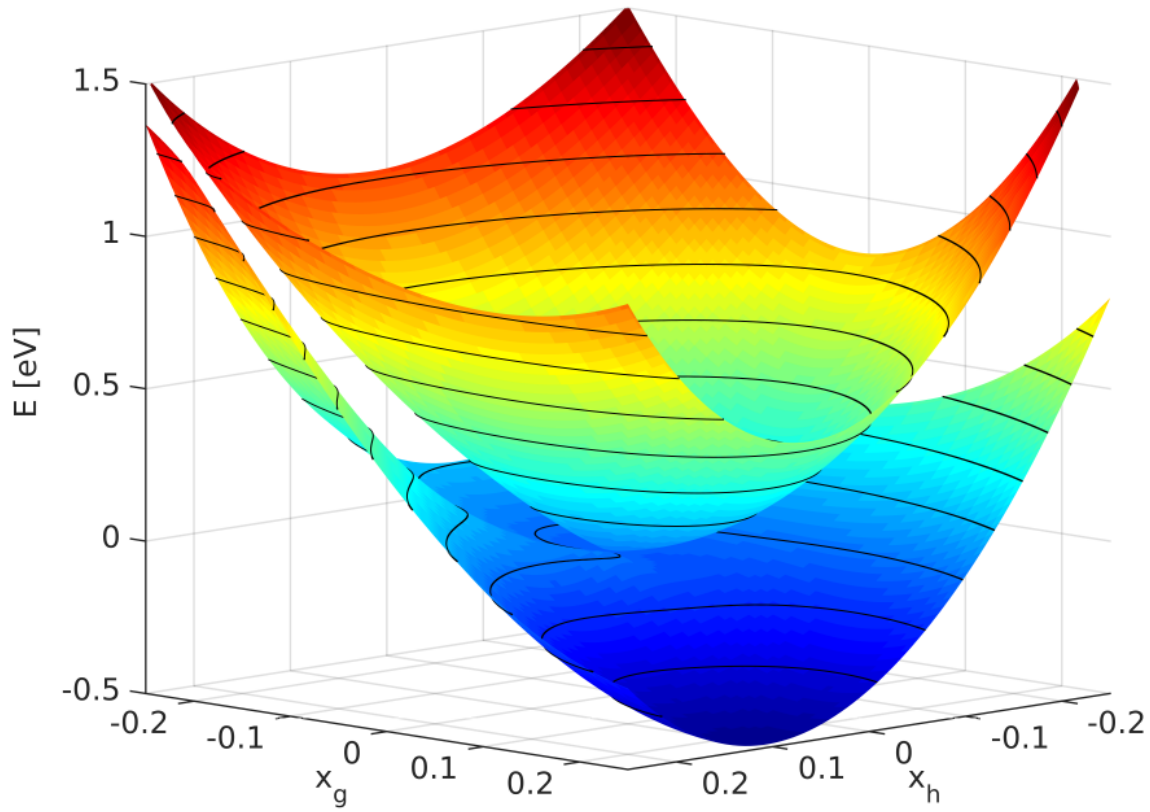

FIG. S3. Adiabatic potential energy surfaces. The conical intersection is in the center of the coordinate system.

where the reduced mass m is 30000 au ($\approx$ 16 amu) for both coordinates and $x = (x_h, x_g)$. The time stepping

$$\psi(x, t + \Delta t) = \exp\left(-iH\Delta t\right)\psi(x, t)\,, \tag{S8}$$

is calculated with the Short Iterative Lanczos (SIL) method [3], and a step size of $\Delta t = 4$ au ($\approx$ 100 as). The corresponding diabatic wave function is expressed in terms of the electronic states:

$$\psi(x, t) = \begin{pmatrix} \phi_1(x, t) \\ \phi_2(x, t) \end{pmatrix} \tag{S9}$$

with the normalization $\langle\psi|\psi\rangle = 1$. The resulting time series $\psi(x, t)$ is used subsequently in the signal calculation.

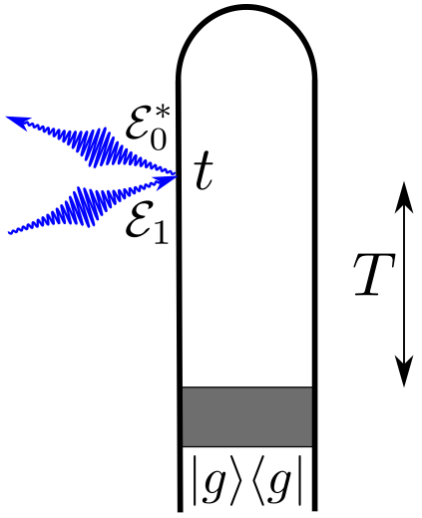

FIG. S4. Loop diagram for TRUECARS. The grey box represents the nonstationary state preparation process after which the system propagates freely for a delay time T before being probed by a Raman process with a hybrid pulse. For diagram rules, see [4].

III. THE SIGNAL

A. TRUECARS signal

The TRUECARS signal can be formally defined as the time-integrated rate of change of photon number in the attosecond (broadband) field $\mathcal{E}_0$

$$S(\omega) = \int \langle \frac{\mathrm{d}}{\mathrm{d}t} \hat{N}^0_\omega(t) \rangle \mathrm{d}t \tag{S10}$$

where the $\hat{N}_\omega$ is the number operator for the photon mode with frequency ω and the 0 superscript indicates restriction to modes occupied by the $\mathcal{E}_0$ pulse. We use the Heisenberg equation of motion for the operator $\hat{N}^0_\omega$ with the interaction Hamiltonian given by

$$\hat{H}_{\mathrm{int}} = \hat{\alpha}(\hat{\mathcal{E}}_0^* \hat{\mathcal{E}}_1 + \hat{\mathcal{E}}_0 \hat{\mathcal{E}}_1^*), \tag{S11}$$

where $\hat{\alpha}$ is the electronic polarizability operator and the electric field operators are

$$\hat{\mathcal{E}}_j = i \sum_{\omega \in \mathcal{E}_j} \sqrt{\frac{2\pi\omega}{\Omega}} \hat{a}_\omega \tag{S12}$$

with Ω the quantization volume. Taking the commutator $[\hat{H}_{\mathrm{int}}, \hat{N}^0_\omega]$ then gives the signal as

$$S(\omega) = 2\Im \int \mathrm{d}t e^{i\omega(t-T)} \mathcal{E}_0^*(\omega) \mathcal{E}_1(t-T) \langle \hat{\alpha}(t) \rangle \tag{S13}$$

where we have taken field expectation values assuming coherent states and thus replaced field operators by field envelopes. The corresponding loop diagram is shown in fig. S4. The dependence of the signal on T comes through the central time of the $\mathcal{E}_1$ pulse which can also be seen as bounding the dt integration. Rewriting the expectation value $\langle \dots \rangle$ explicitly in terms of the wavefunction $|\psi(t)\rangle$ then results in Eq. (2) from the main text. The reduced electronic density matrix is obtained by integrating over the nuclear degrees of freedom:

$$\rho_{el} = \mathrm{Tr}_n(\rho) = \begin{pmatrix} \langle \phi_1 | \phi_1 \rangle & \langle \phi_1 | \phi_2 \rangle \\ \langle \phi_2 | \phi_1 \rangle & \langle \phi_2 | \phi_2 \rangle \end{pmatrix} \tag{S14}$$

From eq. S14, it becomes clear that the coherence of the electronic subsystem, $\rho_{12} = \langle \phi_1(x) | \phi_2(x) \rangle$, is given by the overlap integral of the nuclear wave functions on the two surfaces.

The TRUECARS signal (Eq. (2)) is calculated in the following way. The X-ray transition polarizability α is assumed to be constant in the nuclear coordinate space:

$$\hat{\alpha} = \begin{pmatrix} 0 & 1 \\ 1 & 0 \end{pmatrix} \tag{S15}$$

The time depended material property is then calculated from the wave function obtained from eq. S8:

$$\alpha(t) = \langle \psi(t) | \hat{\alpha} | \psi(t) \rangle = \langle \begin{pmatrix} \phi_1(t) \\ \phi_2(t) \end{pmatrix} | \begin{pmatrix} 0 & 1 \\ 1 & 0 \end{pmatrix} | \begin{pmatrix} \phi_1(t) \\ \phi_2(t) \end{pmatrix} \rangle = 2\Re \langle \phi_1(t) | \phi_2(t) \rangle \tag{S16}$$

The narrowband field is assumed to be of Gaussian shape

$$\mathcal{E}_1(t) = \exp\left(\frac{-t^2}{2\sigma^2}\right) \tag{S17}$$

The wave packet trace of potential energy splitting as it is shown in Fig. 2 is obtained by a weighted energy difference between the adiabatic PESs S_1 and S_2:

$$\Delta V(t) = \frac{\int_{-\infty}^{+\infty} \mathrm{d}x |\Psi_1(x,t)\Psi_2(x,t)| \left(V_2(x) - V_1(x)\right)}{|\langle \Psi_1(x,t) | \Psi_2(x,t) \rangle|} \tag{S18}$$

The adiabatic wave function is obtained by the unitary transformation $U(x)$ that diagonalizes the diabatic PESs:

$$\begin{pmatrix} \Psi_1(x,t) \\ \Psi_2(x,t) \end{pmatrix} = \begin{pmatrix} \cos(\theta(x)) & \sin(\theta(x)) \\ -\sin(\theta(x)) & \cos(\theta(x)) \end{pmatrix} \begin{pmatrix} \phi_1(x,t) \\ \phi_2(x,t) \end{pmatrix} \tag{S19}$$

with the mixing angle θ

$$\tan 2\theta(x) = \frac{1}{2} \frac{H_{12}(x)}{H_1(x) - H_2(x)} \tag{S20}$$

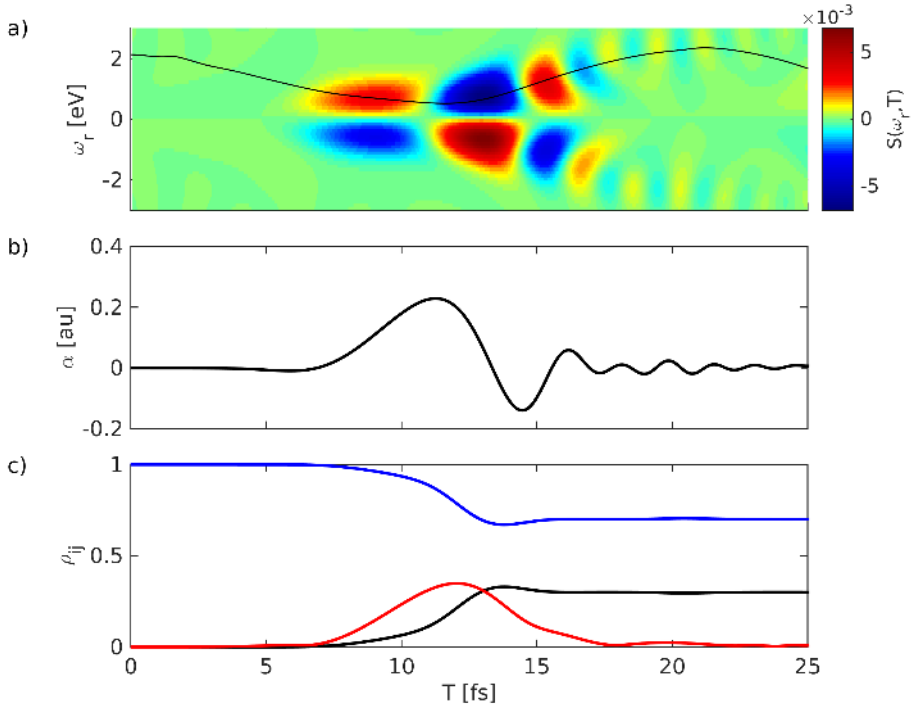

FIG. S5. This is the same figure as Fig. 2 but for different intitial conditions. (a) Simulated nuclear TRUECARS Signal (Eq. 2) for the two-dimensional model with a pulse length of 1.2 fs ($\mathcal{E}_1$). The solid line indicates the average splitting of the potential energy surfaces. (b) The time dependent expectation value of the polarizability. (c) Elements of the reduced density matrix of the electronic subsystem. Blue and black: populations of the adiabatic S_2 and S_1 state respectively. Red line: the magnitude of the electronic coherence.

B. Signal for different initial conditions

Figure S5 shows an alternative simulation for a TRUECARS signal. The Franck-Condon (FC) point is assumed to be at $(0.5, 0.5)$ (In Fig. 2 the FC is $(0.5, 0.0)$). The gradients along the reaction path of the S_1/S_2 surfaces differ significantly more causing a much shorter coherence time than in Fig. 2.

[1] A. M. D. Lee, J. D. Coe, S. Ullrich, M. L. Ho, S. J. Lee, B. M. Cheng, M. Z. Zgierski, I. C. Chen, T. J. Martinez, and A. Stolow, J. Phys. Chem. A **111**, 11948 (2007).

[2] H.-J. Werner, P. J. Knowles, G. Knizia, F. R. Manby, M. Schütz, *et al.*, "Molpro, version 2010.1, a package of ab initio programs," (2010), see http://www.molpro.net.

[3] D. J. Tannor, *Introduction to Quantum Mechanics: A Time-Dependent Perspective* (University Science Books, 2006).

[4] S. Rahav and S. Mukamel, Adv. At. Mol., Opt. Phys. **59**, 223 (2010).